Tunable phononic structures using Lamb waves in a piezoceramic plate

N. Kherraz,[*] F.-H. Chikh-Bled, R. Sainidou,[†] B. Morvan, and P. Rembert
Laboratoire Ondes et Milieux Complexes UMR CNRS 6294, Normandie University, UNIHAVRE, 75 Rue Bellot, 76600 Le Havre, France

(Received 21 November 2018; revised manuscript received 18 January 2019; published 4 March 2019)

Phononic crystals made of piezoceramic materials allow for frequency band structure tunability due to the ease of electric command use. In this paper, we develop a full elastodynamic model, taking into account piezoelectric coupling effects for the band-structure calculation of Lamb eigenmodes of a phononic crystal consisting of a piezoceramic plate with a one-dimensional periodic array of electrodes set on both sides. The dispersion-relation characteristics of these eigenmodes are nondestructively tuned via external circuit impedance loads coupled to the phononic plate, e.g., through inductance loads inducing tunable resonant flat bands that hybridize with the Lamb modes of the elastic plate, thus opening up hybridization gaps. It is shown that additional control of the shape of these resonant bands can be achieved by incorporating an impedance interconnecting two adjacent electrodes of the same side, the whole structure forming an electric quadripole. This behavior can be easily predicted with the help of our formalism combined with a simplified electric line model of the phononic crystal plate.

DOI: 10.1103/PhysRevB.99.094302

I. INTRODUCTION

Phononic crystals and, more recently, elastic metamaterials [1,2] have shown a substantial growth in number of works as well as in modern topics, including heat control [3], topological [4,5], and nonreciprocal [6–8] wave phenomena, inspired, most of the time, from their photonic counterpart [9,10]. Apart from, nowadays, traditional investigations concerning opening and formation of frequency band gaps [11–13], the related research focused on tools to control the propagation of waves in these structures through the engineering of their dispersion properties, associated to interesting issues for applications, such as cloaking [14], filtering [15], sensing [16], waveguiding [17–19], focusing [20], and negative refraction [21] phenomena. Initially, this approach was primitive in the sense that the structure should be redesigned each time a new, different frequency response had to be obtained [22]. In the last decade, these efforts have been oriented to the class of so-called *active* phononic crystals, allowing for a manipulation of waves in a nondestructive manner, relying often on coupling mechanisms such as magnetostrictive or piezoelectric effects. In such a way, the structure behaves at will by tuning its dispersion properties through external parameters, e.g., applied forces [23], electric [24], or magnetic [25,26] fields, temperature-induced crystallization and melting [27] or ferroelectric [28] phase transitions.

Among these excitations, piezoelectric-related effects seem to be the most popular [8,29–42]. Apart from the case of one-dimensional (1D) multilayered stacks including piezoelectric layers [8,29,35–37,41], in most cases, the piezoelectric material is used in the form of an array of patches deposited in an otherwise homogeneous nonpiezoelectric semi-infinite substrate or plate [30,31,34,42]. These studies have been inspired in a large degree from the pioneer work on excitation and sensing of surface acoustic waves [43,44] in the 1960s with applications in the later years to interdigital transducers design [45], shedding light on them by paving the way in several domains such as structural health monitoring, medical imaging, etc.

Although the piezoelectric patches have been extensively used to construct phononic crystals, the role of the patch arrays being either to excite the structure, or to provide local resonances tuned via external circuits, piezoelectric materials have been rarely utilized in phononic crystal plates as a hosting material with embedded or structured inclusions. More recently, some first studies used a piezoceramic material as a host matrix for a 2D holey array [46,47]. Later, a number of works followed, including homogeneous piezoelectric plates with either corrugated surfaces [32,33], or a 1D array of metallic electrode strips printed on these surfaces [38–40]. These studies present frequency band-structure calculations performed through analytical *ab initio* models when dealing with shear horizontal (SH) elastic modes [32,33,48], or they use finite elements simulations (thus losing physical insight) for the description of Lamb modes [38–40], in the absence of a theoretical model adapted for these modes (except for an approximative approach [40]). We know of only one work dealing with a theoretical description of the dispersion of Rayleigh waves in piezoelectric substrates with a periodic array of metallic strips coupled to impedance loads at the interface [49].

A lot of work has been done in uniform piezoelectric plates (with metallized or not surfaces) studying theoretically [50,51] and experimentally [52] Lamb and SH [53] eigenmodes in these structures. The related research has focused mainly on the study of frequency regions close to the cutoff

[*]Present address: Department of Physics and Nanostructured Interfaces & Surfaces Centre, University of Torino, Via Pietro Giuria 1, 10125 Torino, Italy.
[†]sainidor@univ-lehavre.fr

 ©2019 American Physical Society

points (i.e., for small values of the wave-vector components parallel to the plate's characteristic surfaces) [54] for use in characterization of these materials and transducer applications [55–59] on the elaboration of models describing in an effective manner the piezoelectric behavior of the material through electric circuit equivalents [60,61], as well as their transmission and reflection properties [62,63]. Surprisingly, this rich experience has not been transferred to the field of phononic crystals and related structures by incorporating the study of Lamb modes in these structures and the simultaneous development of full elastodynamic theoretical models for their description.

In this paper, we present a theoretical model for the description of Lamb eigenmodes in piezoelectric homogeneous plates, on both surfaces of which arrays of metallic strips are deposited. The phononic crystal plate is embedded in vacuum and external circuits are also considered, coupled to the electrodes. Our formalism employs Fourier series expansions incorporated in the basic equations of linear piezoelectricity, to derive, at a first stage, the frequency band structure of the Lamb-like eigenmodes of such a structure, and shows that nondestructive control and tunability in their frequency response become feasible. In particular, we show that an external electric quadripole interconnecting adjacent cells of the crystals offers an additional degree of freedom compared to single dipole loads to shape the resonance-induced hybridization gaps opening up in their frequency band structure.

Our paper, apart from its utility in the development of theoretical tools relying on a full elastodynamic description that takes into account piezoelectric coupling effects, beyond any effective descriptions based on 1D mass-spring analogs or equivalent electric circuits for the modeling of Lamb wave propagation in piezoelectric phononic plates, could also be of interest for use in a characterization process using the dispersion of eigenmodes along the direction of the surfaces of the piezoelectric plate.

The paper is organized as follows. First, the theoretical model used for the study of piezoelectric phononic crystal plates is developed in Sec. II and, next, in Sec. III we present some examples demonstrating the applicability of our formalism and offering possibilities to drastically modify the band structure of these plates. Finally, Sec. IV concludes the paper.

II. THEORETICAL MODEL

A. Phononic structure description

We shall develop a theoretical model for the calculation of the frequency band structure of an infinite, 1D phononic crystal made of a lead zirconate titanate (PZT) plate with 6*mm* crystal symmetry on both sides of which parallel metallic strips (electrodes) of negligible thickness are deposited periodically along x_1 direction. We will focus on the dispersion relation $\omega(k_1)$ of Lamb-like eigenmodes of angular frequency ω propagating along x_1 with a Bloch wave vector $\mathbf{k}_1 = k_1\hat{\mathbf{x}}_1$; the SH elastic modes, polarized along x_2 axis, will not concern us here. The plate of finite thickness h is considered to extend to infinity in x_1x_2 plane and it is centered along x_3 axis (extending from $-h/2$ to $h/2$), as shown in Fig. 1. The electrodes are of width w, with s the separation distance between adjacent

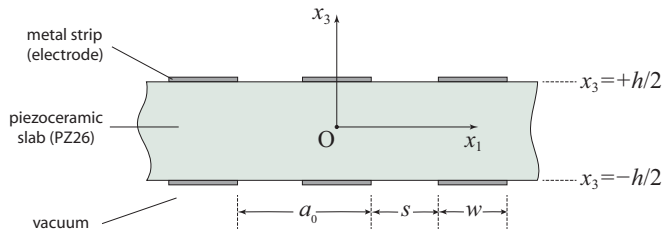

FIG. 1. Schematic representation of the one-dimensional piezoelectric crystal, extending to infinity along x_1 and x_2 directions, which coincide with the transversely isotropic plane of the piezoceramic material, poled across its thickness along the x_3 symmetry axis. The metallic strips of width w and with separation gap s, aligned in parallel to x_2, form a geometric array along x_1 with period $a_0 = s + w$.

electrodes. The lattice constant of the crystal is $a_0 = s + w$ in this simplest case. It is, however, worth noting that each electrode can be connected to an electric circuit, i.e., loaded with an impedance, and this load may be identical or differ for the up and down side, for adjacent electrodes, and/or connect more than one consecutive electrodes. We will call these loads electric boundary conditions (EBCs), whose variability and flexibility in a nondestructive for the whole structure manner, offers a degree of freedom to tune and control the periodicity and response of the phononic crystal. Of course, in these more complex cases, the unit cell of the crystal will include several elementary blocks of length a_0, thus the lattice constant a will be a multiple of a_0.

B. Fundamental equations

Within a bulk piezoelectric material whose elastic properties are described by its elastic parameters (mass density ρ and elastic coefficients c_{ijkl}) and its electric properties by the permittivity tensor elements ϵ_{ik}, the two field subspaces, the elastic strain field **S**, and the electric field **E**, are interacting; their coupling is described by the piezoelectric constants e_{ikl}. The constitutive equations in the framework of linear piezoelectricity, combining Maxwell equations and Hooke's law in a generalized form, are

$$T_{ij} = c^E_{ijkl}S_{kl} - e_{kij}E_k, \tag{1}$$

$$D_i = e_{ikl}S_{kl} + \epsilon^S_{ik}E_k, \tag{2}$$

relating the stress tensor components T_{ij} and the electric displacement vector components D_i, to both the strain tensor S_{kl} and the electric field components E_k; c^E_{ijkl} and ϵ^S_{ik} denote, respectively, the elastic coefficients under constant electric field, and the permittivity tensor elements under constant strain. **T** and **D** satisfy the stress equation of motion (we assume monochromatic waves of angular frequency ω with a $e^{+i\omega t}$ time-dependence),

$$T_{ij,i} = \rho\ddot{u}_j = -\rho\omega^2 u_j, \tag{3}$$

and the charge equation of electrostatics

$$D_{i,i} = 0. \tag{4}$$

In the absence of coupling, the piezoelectric constants e_{ikl} become zero and Eqs. (1) and (2) drop to two independent subspaces (the elastic and electric fields become independent). In the above equations and throughout the paper, we adopt Einstein's summation rule, and we use the notation $(\cdot)_{,j} \equiv \frac{\partial(\cdot)}{\partial x_j}$ to denote partial derivatives with respect to cartesian coordinates x_j, $j = 1, 2, 3$, which coincide with the high-symmetry directions of the PZT piezoceramic materials that will concern us here. Instead of the primary, strain and electric, fields appearing in Eqs. (1), (2) we find it convenient to use the elastic displacement field $\mathbf{u}$ and the scalar electric potential φ, given by

$$E_k = -\varphi_{,k}, \tag{5}$$

$$S_{ij} = \tfrac{1}{2}(u_{i,j} + u_{j,i}), \tag{6}$$

and we construct a generalized elastic displacement vector by expanding it to a 4D space, the fourth component being the electric potential, i.e., $\mathbf{u} = [u_1\ u_2\ u_3\ u_4 = \varphi]^t$. Since the SH modes ($u_2$) are decoupled from the Lamb-like and electric potential components (u_i, $i = 1, 3, 4$), we will omit, hereafter, all relevant components along x_2 axis (we put $u_2 = 0$).

C. Elementary solutions

In this paper, we focus on a specific class of piezoelectric materials, the PZT piezoceramics, known to exhibit high piezoelectric constants and low loss. Explicit forms for their elastic, piezoelectric, and dielectric tensors are given in Appendix A. For the calculation of the eigenmodes of the piezoelectric phononic crystal we need, first, to determine the elementary solutions of the bulk material. Due to the planar geometry of the structure, we will assume monochromatic plane-wave solutions of angular frequency ω propagating along x_1 with a time dependence of the form $e^{+i\omega t}$ tacitly assumed in all wave fields, but omitted to simplify notation. These solutions are characterized, for given ω, by a given wave-vector component projection $\mathbf{k}_1 = +\omega s_1 \hat{\mathbf{x}}_1$ and by the polarization index $p = 1, 2, 3$, accounting for three—one longitudinal and two transverse—elastic waves whose wave-vector projection along x_3 axis is $\mathbf{k}_3^{\pm(p)} = \pm\omega s_3^{(p)} \hat{\mathbf{x}}_3$, where s_1 and $s_3^{(p)}$ are the slowness vector components along x_1 and x_3 axes, respectively. The generalized elastic field takes the form $u_i = e^{-i\omega s_1 x_1} \sum_p (B_i^{+(p)} e^{-i\omega s_3^{(p)} x_3} + B_i^{-(p)} e^{+i\omega s_3^{(p)} x_3})$, where $i = 1, 3, 4$, and, $B_i^{\pm(p)}$ are appropriate coefficients for the elastic waves propagating along $\pm\hat{\mathbf{x}}_3$ directions. Both $s_3^{(p)}$ and $B_i^{\pm(p)}$ are perfectly known, for the case of the bulk piezoelectric material, and for a given s_1 value are found by solving a nonlinear eigenvalue problem, with eigenvalues $s_3^{(p)}$ and corresponding eigenvectors $\mathbf{B}^{\pm(p)}$, the polarization index p numbering the eigenvalues, as detailed in Appendix A.

The periodicity along x_1 direction implies that the Lamb-like eigenmodes of the phononic crystal plate will be expanded in the basis of the elementary solutions of the corresponding bulk material, as described above, each of them characterized by a wave-vector component $\mathbf{k}_{1n} = +\omega s_{1n} \hat{\mathbf{x}}_1 = k_1 \hat{\mathbf{x}}_1 + \mathbf{g}_n$, where k_1 is the reduced wave-vector component within the first Brillouin zone (BZ) $[-\frac{\pi}{a}, \frac{\pi}{a}]$ and $\mathbf{g}_n = \frac{2\pi}{a} n \hat{\mathbf{x}}_1 \equiv g_n \hat{\mathbf{x}}_1$, with $n = 0, \pm 1, \pm 2, \ldots$, are the reciprocal lattice vectors, generating several diffracted beams of slowness component $s_{3n}^{(p)}$ along x_3 direction. We write the generalized elastic field within the plate ($|x_3| \leqslant \frac{h}{2}$) as

$$u_i = \sum_{n=-\infty}^{+\infty} e^{-i\omega s_{1n} x_1} \sum_p \left(C_n^{+(p)} B_{\text{in}}^{+(p)} e^{-i\omega s_{3n}^{(p)} x_3} + C_n^{-(p)} B_{\text{in}}^{-(p)} e^{+i\omega s_{3n}^{(p)} x_3} \right), \quad i = 1, 3, 4, \tag{7}$$

which satisfies the Bloch-Floquet theorem; $s_{3n}^{(p)}$ and $B_{\text{in}}^{+(p)}$ are determined for given s_{1n} from the bulk properties (see Appendix A). Without loss of generality, we choose $B_{1n}^{-(p)} = B_{1n}^{+(p)}$, while the other components must obey $B_{\text{in}}^{-(p)} = -B_{\text{in}}^{+(p)}$ for $i = 3, 4$, as can be easily seen if we replace $s_{3n}^{(p)} \to -s_{3n}^{(p)}$ in Eq. (A8). The unknown coefficients $C_n^{\pm(p)}$ are to be determined, with the help of the appropriate boundary conditions applied to the interfaces of the plate, located at $x_3 = \pm\frac{h}{2}$.

In a similar manner, we develop the field in the regions outside the plate. We note that, first, in the outer region of the plate (vacuum) only electromagnetic waves exist (the elastic field components vanish) and the slowness vector component along x_3 axis takes the form $s_{3n}^2 = \frac{1}{c_0^2} - s_{1n}^2 \approx -s_{1n}^2$, where $c_0 = 3 \cdot 10^8$ m s^{-1} is the propagation velocity of electromagnetic waves in vacuum, and s_{1n} is a conserved quantity across the phononic crystal structure with typical values much higher than c_0^{-2}. Second, the electric potential component must decay away from the plate (we consider a pseudoeigenvalue problem, with leaky electric waves). We write the generalized elastic field outside the plate,

$$u_i^{\nu} = \begin{cases} \varphi^{\nu} = \sum_{n=-\infty}^{+\infty} C_n^{\nu} e^{-i\omega(s_{1n}x_1 + s_{3n}|x_3|)}, & i = 4 \\ 0, & i = 1, 2, 3, \end{cases} \tag{8}$$

with $\nu = \text{u}, \text{d}$ denoting, respectively, the upper ($x_3 > \frac{h}{2}$) and lower ($x_3 < -\frac{h}{2}$) outer region, and $s_{3n} \approx -i\xi_n s_{1n}$, where $\xi_n = +1$ if $\text{Re}\{s_{1n}\} \geqslant 0$ and $\xi_n = -1$ elsewhere, to always ensure evanescent behavior along x_3 direction for both sides of the plate. Since all wave fields must satisfy Bloch's theorem, x_1 will be restricted hereafter within the first unit cell ($|x_1| \leqslant \frac{a}{2}$) without any loss of generality.

The next step is the matching of the wave fields of the outer and inner regions at the two surfaces of the plate. The presence of the electrodes will not modify the elastic boundary conditions, because we assume the electrodes to be of negligible thickness with respect to the plate's thickness and to the skin depth of the metal (to neglect losses in their interior). The surfaces are considered to be traction free at any point, i.e.,

$$T_{33}(x_3 = \pm h/2) = 0, \quad T_{31}(x_3 = \pm h/2) = 0, \tag{9}$$

where T_{33}, T_{31} are the stress normal and tangential, respectively, components at $x_3 = \pm h/2$. In addition, the electric field tangential component is continuous across the interfaces

$$E_1 = E_1^{\nu}, \quad \text{for} \quad x_3 = \pm h/2, \tag{10}$$

while the normal component of the electric displacement field must satisfy the Maxwell-Gauss equation across the interfaces

$$D_3^{\nu} - D_3 = \sigma(x_1), \quad \text{for} \quad x_3 = \pm h/2, \tag{11}$$

with $\sigma(x_1)$ being the surface charge density, depending on the presence or not of an electrode at point x_1 and supposed to be uniform on it,

$$\sigma(x_1) = \begin{cases} \sigma^{\nu}, & |x_1| \leqslant \frac{w}{2} \\ 0, & \frac{w}{2} < |x_1| \leqslant \frac{a}{2}, \end{cases} \tag{12}$$

where we have considered the electrodes to be centered at the surfaces of each unit cell. A comment has to be made here: The surface charge density is assumed uniform within the whole electrode area [45], since the electromagnetic wavelengths are much higher than the electrode width w in the frequency range under consideration ($\frac{\omega}{2\pi} \lesssim 1$ MHz) for millimeter-scaled arrays that will concern us here.

The set of the above four boundary conditions [Eqs. (9)–(11)] allow the determination of the unknown coefficients $C_n^{\pm(p)}$ and C_n^{ν}, by taking advantage of the orthogonality properties of the basis of elementary solutions $u_n(x_1) \equiv \mathrm{e}^{-\mathrm{i}\omega s_{1n} x_1}$:

$$\langle u_m, u_n \rangle \equiv \int_{-a/2}^{+a/2} u_m^* u_n \, dx_1 = a\,\delta_{nm}. \tag{13}$$

In practice, the infinite sums in the generalized field expressions Eqs. (7) and (8) are truncated to a maximum value, $n_{\max}$, for the summation index (corresponding to $2n_{\max}+1$ reciprocal lattice vectors).

Combining Eqs. (5) and (10) and defining $\kappa^{\nu} = +1(-1)$ for $\nu = \mathrm{u(d)}$, we obtain—after projection onto the $u_n(x_1)$ basis—the $2 \times (2n_{\max}+1)$ coefficients of the electric potential in the outer region, C_n^{ν},

$$C_n^{\nu} = \sum_{p=1}^{3} B_{4n}^{+(p)} \big(C_n^{+(p)} \mathrm{e}^{-\mathrm{i}\omega\kappa^{\nu} s_{3n}^{(p)} h/2} - C_n^{-(p)} \mathrm{e}^{+\mathrm{i}\omega\kappa^{\nu} s_{3n}^{(p)} h/2} \big) \mathrm{e}^{\mathrm{i}\omega s_{3n} h/2}, \tag{14}$$

as a function of $C_n^{\pm(p)}$ which can be found from the three remaining boundary conditions [Eqs. (9), (11)] as follows. Substituting Eqs. (6) and (7) into Eqs. (1) and (2), we obtain

$$T_{33} = \sum_{n=-\infty}^{\infty} \mathrm{e}^{-\mathrm{i}\omega s_{1n} x_1} \sum_{p=1}^{3} U_n^{(p)} \big(C_n^{+(p)} \mathrm{e}^{-\mathrm{i}\omega s_{3n}^{(p)} x_3} + C_n^{-(p)} \mathrm{e}^{+\mathrm{i}\omega s_{3n}^{(p)} x_3} \big), \tag{15}$$

$$T_{31} = \sum_{n=-\infty}^{\infty} \mathrm{e}^{-\mathrm{i}\omega s_{1n} x_1} \sum_{p=1}^{3} V_n^{(p)} \big(C_n^{+(p)} \mathrm{e}^{-\mathrm{i}\omega s_{3n}^{(p)} x_3} - C_n^{-(p)} \mathrm{e}^{+\mathrm{i}\omega s_{3n}^{(p)} x_3} \big), \tag{16}$$

$$D_3 = \sum_{n=-\infty}^{\infty} \mathrm{e}^{-\mathrm{i}\omega s_{1n} x_1} \sum_{p=1}^{3} X_n^{(p)} \big(C_n^{+(p)} \mathrm{e}^{-\mathrm{i}\omega s_{3n}^{(p)} x_3} + C_n^{-(p)} \mathrm{e}^{+\mathrm{i}\omega s_{3n}^{(p)} x_3} \big), \tag{17}$$

where

$$\begin{aligned} U_n^{(p)} &= -\mathrm{i}\omega \big[c_{13}^E B_{1n}^{+(p)} s_{1n} + c_{33}^E B_{3n}^{+(p)} s_{3n}^{(p)} + e_{33} B_{4n}^{+(p)} s_{3n}^{(p)} \big], \\ V_n^{(p)} &= -\mathrm{i}\omega \big[c_{44}^E B_{1n}^{+(p)} s_{3n}^{(p)} + c_{44}^E B_{3n}^{+(p)} s_{1n} + e_{15} B_{4n}^{+(p)} s_{1n} \big], \\ X_n^{(p)} &= -\mathrm{i}\omega \big[e_{31} B_{1n}^{+(p)} s_{1n} + e_{33} B_{3n}^{+(p)} s_{3n}^{(p)} - \epsilon_{33}^S B_{4n}^{+(p)} s_{3n}^{(p)} \big]. \end{aligned} \tag{18}$$

An expression similar to Eq. (17) can be found for $D_3^{\nu} = -\epsilon_0 \varphi_{,3}^{\nu}$ with the help of Eqs. (8) and (14):

$$D_3^{\nu} = \epsilon_0 \mathrm{i}\omega\kappa^{\nu} \sum_{n=-\infty}^{\infty} s_{3n} \mathrm{e}^{-\mathrm{i}\omega[s_{1n}x_1 + s_{3n}(|x_3| - h/2)]} \times \sum_{p=1}^{3} B_{4n}^{+(p)} \big(C_n^{+(p)} \mathrm{e}^{-\mathrm{i}\omega\kappa^{\nu} s_{3n}^{(p)} h/2} - C_n^{-(p)} \mathrm{e}^{+\mathrm{i}\omega\kappa^{\nu} s_{3n}^{(p)} h/2} \big). \tag{19}$$

Use of these expressions into Eqs. (9) and (11) leads—after projection onto the $u_n(x_1)$ basis—to the following linear system of $6 \times (2n_{\max}+1)$ equations with unknowns $C_n^{\pm(p)}$, denoted in vector form by $\mathbf{C}$:

$$\widetilde{\mathbf{M}}(\omega, k_1)\mathbf{C} = \mathbf{0}. \tag{20}$$

The nontrivial solutions of Eq. (20) are found from the condition $\det \widetilde{\mathbf{M}}(\omega, k_1) = 0$, providing us with the dispersion relation $\omega(k_1)$ of the Lamb-like modes of the phononic crystal plate, lying on x_1x_3 plane and propagating along x_1 axis.

It is worth noting that all the information concerning the EBCs, including impedance loads applied to the electrodes, is involved in the relation for the electric displacement field across the interface [Eqs. (11) and (12)] through the specific form of the surface charge density σ. We will analyze in more detail the way to proceed in dealing with this part of the model in what follows.

D. Electric boundary conditions

The EBC Eqs. (11) concerning the electric displacement field is not, in its present form, of practical interest, if someone needs to introduce impedance loads through external circuits. Instead, the physical quantity, more convenient for this purpose, is the electric potential, therefore Eqs. (11) must be transformed into an equivalent potential form [49].

Let us suppose the general case depicted in Fig. 2(a) with both upper- and lower-side electrodes loaded with external circuits of impedance Z^{u} and Z^{d}, respectively. From Eq. (14) it is obvious to see that the condition to be satisfied at the surfaces of the plate is continuity of the electric potential as a consequence of the electric field boundary condition Eq. (10). For the part of the plate surfaces, covered by the electrodes, we take into account the external circuit [see Fig. 2(b)] and after integration over the surface of the electrodes $\mathcal{A} = wl$, l being the length of the electrodes along x_2 axis [see Eqs. (11) and (12)] we obtain

$$\begin{aligned} \varphi|_{x_3=\pm\frac{h}{2}} &= \Phi_e^{\nu} = -\mathrm{i}\omega Z^{\nu} Q^{\nu} \\ &= -\mathrm{i}\omega Z^{\nu} \iint dx_1\, dx_2 \big(D_3^{\nu} - D_3 \big)\big|_{x_3=\pm\frac{h}{2}} \\ &= -\mathrm{i}\omega Z^{\nu} \mathcal{A} \frac{1}{w} \int_{-\frac{w}{2}}^{+\frac{w}{2}} dx_1 \big(D_3^{\nu} - D_3 \big)\big|_{x_3=\pm\frac{h}{2}}, \end{aligned} \tag{21}$$

where Q^{ν} and Z^{ν} are, respectively, the electric charge in the electrode and the impedance load on it, and Φ_e^{ν} the corresponding external electric potential. We choose to replace $D_3^{\nu}|_{x_3=\pm\frac{h}{2}}$ by $+\epsilon_0(k_1\varphi - \varphi_{,3}^{\nu} - k_1\varphi)|_{x_3=\pm\frac{h}{2}}$ from which

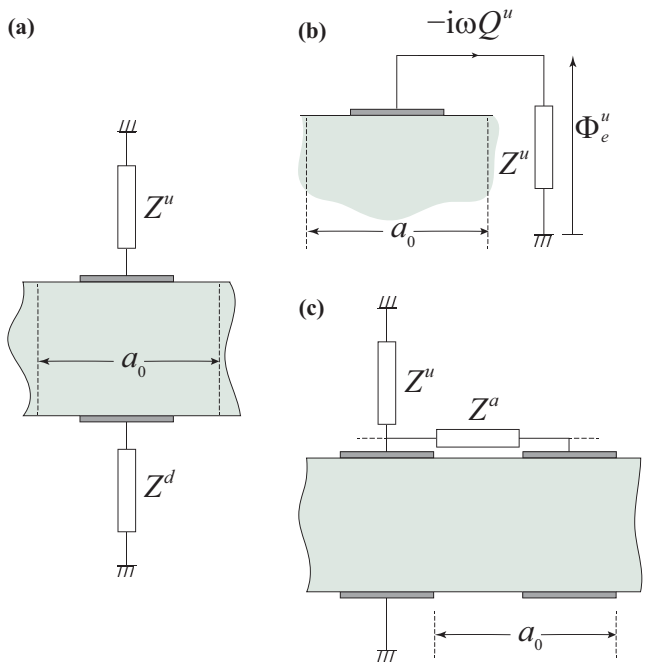

FIG. 2. (a) Schematic representation of a unit cell of the piezoelectric phononic crystal plate, loaded on both sides by external circuits with $Z^{\rm u}$ (upper-side electrode) and $Z^{\rm d}$ (lower-side electrode). Each external circuit imposes an external electric potential Φ_e^ν and the associated electric current, resulting from the impedance load of the circuit, as detailed in (b) for the upper-side electrode. The case of external loads combined with interconnected adjacent electrodes, shown in (c), corresponds to quadripoles that can be effectively described by an equivalent electric dipole of impedance $Z^{\rm u}_{\rm eq}$ (see text), as the one depicted in (a) with $Z^{\rm d}=0$.

we obtain

$$\frac{1}{i\omega Z^\nu \mathcal{A}}\Phi_e^\nu = -\epsilon_0 k_1 \Phi_e^\nu + \epsilon_0 k_1 \frac{1}{w}\int_{-\frac{w}{2}}^{+\frac{w}{2}} dx_1 \times \left(\frac{1}{\epsilon_0 k_1}D_3 + \frac{1}{k_1}\varphi^\nu_{,3} + \varphi\right)\Big|_{x_3=\pm\frac{h}{2}},$$

or, equivalently,

$$\varphi|_{x_3=\pm\frac{h}{2}} = \Phi_e^\nu = \left(1+\frac{1}{i\omega Z^\nu \mathcal{A}\epsilon_0 k_1}\right)^{-1}\frac{1}{w}\int_{-\frac{w}{2}}^{+\frac{w}{2}} dx_1 \times \left(\frac{1}{\epsilon_0 k_1}D_3 + \frac{1}{k_1}\varphi^\nu_{,3} + \varphi\right)\Big|_{x_3=\pm\frac{h}{2}}. \quad (22)$$

Thus, Eqs. (11) have been transformed into a potential relation, for $|x_1| \leqslant \frac{w}{2}$.

For the part of the plate surfaces free of electrodes ($\frac{w}{2} < |x_1| \leqslant \frac{a}{2}$), Eqs. (11) and (12) imply $(D_3^\nu - D_3)|_{x_3=\pm\frac{h}{2}} = 0$. Following again the same hint for D_3^ν as for the surface region inside the electrodes, we can write

$$\varphi|_{x_3=\pm\frac{h}{2}} = \left(\frac{1}{\epsilon_0 k_1}D_3 + \frac{1}{k_1}\varphi^\nu_{,3} + \varphi\right)\Big|_{x_3=\pm\frac{h}{2}}. \quad (23)$$

Equations (22) and (23), combined together, constitute a unique boundary condition for the electric potential, $\varphi|_{x_3=\pm\frac{h}{2}}$, spanning over the entire surface region of the unit cell, and, most importantly, its right-hand side depends, for both subregions inside and outside the electrodes, on the common quantity $(\frac{1}{\epsilon_0 k_1}D_3 + \frac{1}{k_1}\varphi^\nu_{,3} + \varphi)|_{x_3=\pm\frac{h}{2}}$. The latter, by making use of Eqs. (17), (7), (8), and (14), can be expanded into the $u_n(x_1)$ basis set with appropriate expansion coefficients as follows:

$$\left(\frac{1}{\epsilon_0 k_1}D_3 + \frac{1}{k_1}\varphi^\nu_{,3} + \varphi\right)\Big|_{x_3=\pm\frac{h}{2}} = \frac{1}{\epsilon_0 k_1}\sum_{n=-\infty}^{\infty} e^{-i\omega s_{1n}x_1}\sum_{p=1}^{3}\left(C_n^{+(p)}\mathcal{F}_n^{+(p)\nu}e^{-i\omega\kappa^\nu s_{3n}^{(p)}h/2} + C_n^{-(p)}\mathcal{F}_n^{-(p)\nu}e^{+i\omega\kappa^\nu s_{3n}^{(p)}h/2}\right), \quad (24)$$

with

$$\mathcal{F}_n^{\pm(p)\nu} = X_n^{(p)} \mp B_{4n}^{+(p)}\epsilon_0[(\kappa^\nu\xi_n - 1)k_1 + \kappa^\nu\xi_n g_n]. \quad (25)$$

The final form for $\varphi|_{x_3=\pm\frac{h}{2}}$, after projection onto the $u_n(x_1)$ basis set leads to $2\times(2n_{\max}+1)$ equations,

$$\sum_n\sum_{p=1}^{3}\left\{C_n^{+(p)}\left[\gamma^\nu_{nm}\mathcal{F}_n^{+(p)\nu} - a\delta_{nm}B_{4n}^{+(p)}\right]e^{-i\omega\kappa^\nu s_{3n}^{(p)}h/2} + C_n^{-(p)}\left[\gamma^\nu_{nm}\mathcal{F}_n^{-(p)\nu} + a\delta_{nm}B_{4n}^{+(p)}\right]e^{+i\omega\kappa^\nu s_{3n}^{(p)}h/2}\right\} = 0, \quad (26)$$

where the coefficients γ^ν_{nm} result from the integration performed over x_1 and include the information about impedance loads (see Appendix B); δ_{nm} is the Kronecker delta. Equation (26) constitutes a nondiagonal, in the $\{n\}$-space, subset of Eq. (20), corresponding to the electric part of the applied boundary conditions (EBCs). The remaining $4\times(2n_{\max}+1)$ equations, derived from Eqs. (15) and (16) and already included in Eq. (20), are diagonal in $\{n\}$-space and correspond to the purely mechanical, uniform along x_1, boundary conditions [Eqs. (9)].

We close this part by including the specific case of an external circuit interconnecting adjacent electrodes through an additional impedance load Z^a [see Fig. 2(c)]. For simplicity, we assume this load to be applied only at one side of the plate (let's say the upper part) while the other-side electrode is grounded, but this scheme can be easily extended to include various circuit combinations to the upper and lower electrodes. From elementary electric circuit considerations, it is obvious to see that the quadripole of Fig. 2(c) is equivalent to a single impedance load $Z^{\rm u}_{\rm eq}$ given by

$$Z^{\rm u}_{\rm eq} = \frac{Z^{\rm u}}{1+\frac{Z^{\rm u}}{Z^a}\left(2\sin\frac{k_1 a}{2}\right)^2}. \quad (27)$$

Equation (27) offers a versatile tool for the enhancement of intercellular interactions, as we demonstrate in Sec. III C for the case of capacitance loads ($Z^a = 1/iC_a\omega$).

Though the electric circuit configurations that we have treated have the same periodicity as the metallic strip array ($a = a_0$), our formalism can be easily generalized to include EBCs spanning over more than one elementary block ($a = \kappa a_0$, $\kappa = 2, 3, \ldots$) by appropriately performing the integration along x_1. Of course, by the same token, electrodes of a unit cell that differ in size and position for the upper and

TABLE I. Material parameters for PZ26, used in the calculations.

Material property	Symbol	Value
Elastic coefficients c^E_{pq} [GPa]	c^E_{11}	175.0
	c^E_{12}	110.3
	c^E_{13}	95.0
	c^E_{33}	124.0
	c^E_{44}	26.3
	$c^E_{66} = \frac{1}{2}(c^E_{11} - c^E_{12})$	32.3
Piezoelectric coefficients e^S_{ip} [C m^{-2}]	e^S_{15}	10.00
	e^S_{31}	−2.62
	e^S_{33}	16.48
Relative permeability coefficients ϵ^S_{pq}	ϵ^S_{11}	800.0
	ϵ^S_{33}	767.6
Mass density [kg m^{-3}]	ρ	7700

lower side of the plate can be also considered in the formalism presented here.

III. SOME EXAMPLES

To demonstrate the applicability of our method, we consider some examples containing, first, symmetric with respect to x_1x_2-plane EBCs, and, second, asymmetric with respect to x_1x_2-plane EBCs for the specific case of an inductance load, combined or not, with a capacitance. The infinite 1D phononic crystal plate consists, as already described, of an array of identical metallic strips deposited symmetrically on both sides of the plate of thickness $h = 2.2$ mm. The electrodes, of width $w = 1.7$ mm and separation distance $s = 0.3$ mm, form in the simplest case a lattice along x_1 axis, with spatial period $a_0 = s + w = 2$ mm. The plate itself is made of PZ26, a piezoceramic material with high coupling piezoelectric constants. Its parameters, used in the calculations, are summarized in Table I. We note that all bands shown in our calculations are real in the sense that the imaginary part of the wave number is lower than 0.005 of the corresponding real part. Absorption is not taken into account in elastic nor electric coefficients of the plate material; however, losses are indirectly included through external leakage of EM waves even if negligible. Additionally, if the presence of an outer medium (fluid) is considered, Im$\{k_1\}$ may be higher. In a real experiment, of course, losses are present and the above formalism can be directly used, by just including appropriate imaginary parts in all elastic, electric, and piezoelectric coefficients. For PZT materials as those considered in our study for the band-structure calculations, these imaginary parts are of the order of 10^{-2} with respect to the corresponding real parts [64].

A. Nonresonant symmetric EBCs

To begin, we apply symmetric EBCs to both up and down electrodes of each elementary cell of length a_0, for two extreme for the impedance cases, i.e., floating-potential conditions ($Z^{\rm u} = Z^{\rm d} \to \infty$), and, grounded electrodes ($Z^{\rm u} = Z^{\rm d} = 0$). In both configurations, the period of the EBCs coincides with the spatial period of the metallic strip array ($a = a_0$).

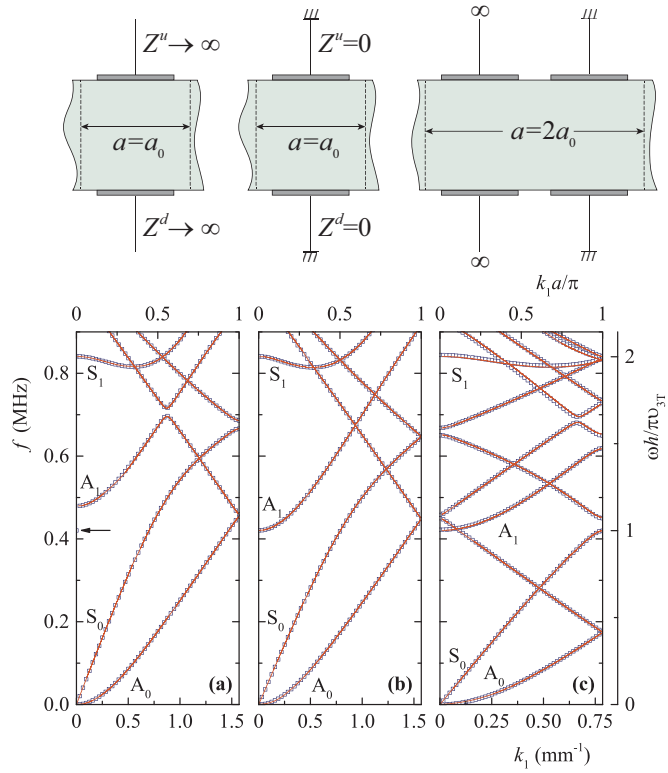

FIG. 3. Calculated frequency band structure (solid lines) of an infinite one-dimensional phononic crystal plate consisting of an array of metallic strips of width $w = 1.7$ mm along x_1 axis, aligned along x_2 axis, and deposited on both sides, with separation distance $s = 0.3$ mm and spatial period $a_0 = s + w = 2$ mm, for several configurations of symmetric EBCs applied to the electrodes, as depicted schematically at the top of the plots: (a) floating potential conditions ($Z^{\rm u} = Z^{\rm d} \to \infty$) in all elementary cells, (b) grounded electrodes ($Z^{\rm u} = Z^{\rm d} = 0$) in all elementary cells, and (c) EBCs spanning over two adjacent elementary cells, alternating grounded and floating-potential conditions. Finite element calculations are also shown (open symbols) for comparison.

The calculated frequency band structure along x_1 direction is shown (solid lines) in Figs. 3(a) and 3(b), respectively, for these two simple systems, following the procedure described in Sec. II, for the resolution of the nonlinear eigenvalue problem Eq. (20). Only the positive k_1 axis is shown, since the band structure diagrams are invariant under the substitution $k_1 \to -k_1$, for all the cases considered in this paper. For the first, floating-potential crystal [Fig. 3(a)], the lowest-frequency, A_0-like, branch is folded due to the periodicity at about 0.45 MHz and the folded negative-slope branch interacts slightly with the A_1-like branch with cutoff frequency at about 0.48 MHz, thus opening up a narrow hybridization gap centered at 0.7 MHz. Next, the S_0-like branch, linear at the long-wavelength limit, is folded at the first BZ edge, at about 0.68 MHz, opening up a small Bragg-type gap. Finally, the S_1-like mode is generated with cutoff frequency at about 0.82 MHz. A similar picture is observed for the second, grounded crystal [Fig. 3(b)]. The most striking differences as

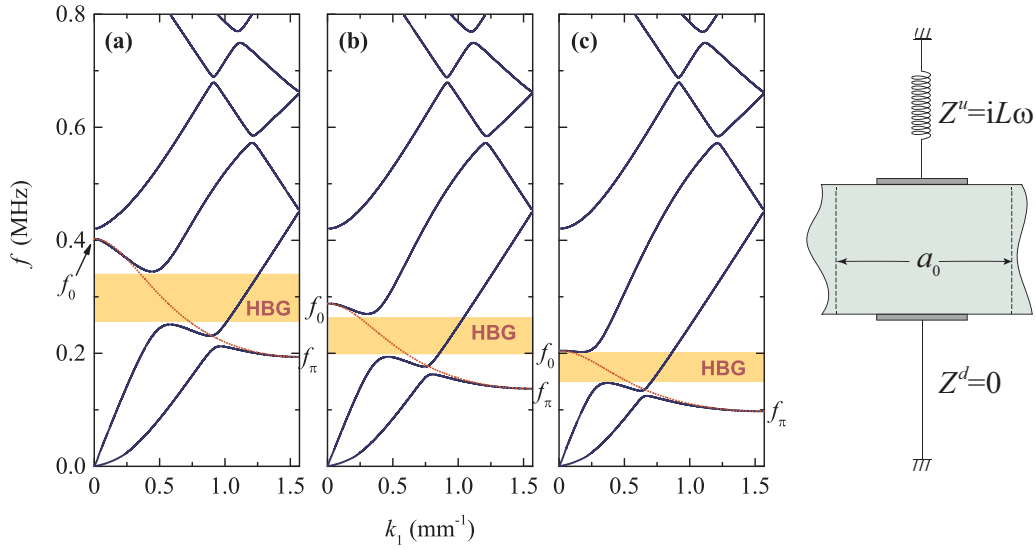

FIG. 4. Calculated frequency band structure (solid lines) of an infinite one-dimensional phononic crystal plate, as described in Fig. 3, but with asymmetric EBCs applied shown in the right margin, consisting of grounded electrodes at the lower plate surface ($Z^{\rm d}=0$) and inductance loaded electrodes at the upper plate surface ($Z^{\rm u}=\mathrm{i}L\omega$), for different values of the inductance load: (a) $L=235$ μH, (b) $L=470$ μH, and (c) $L=940$ μH. The dotted lines represent electric resonance bands before hybridization (see text) leading to hybridization band gaps (HBG) for the S_0-like modes (shaded areas) after hybridization.

compared to the previous case are the red-shifted cutoff frequency for the A_1-like mode, whose value coincides with the isolated point solution of Fig. 3(a), indicated by an arrow, and, the weaker interactions leading to even narrower frequency band gaps.

As a last case, we build a crystal with a more complex unit cell, combining the two above-mentioned cases. The EBCs span over two elementary adjacent cells, i.e., $a=2a_0$, the first having floating potential ($Z_1^{\rm u}=Z_1^{\rm d}\to\infty$), the second being grounded ($Z_2^{\rm u}=Z_2^{\rm d}=0$). Such complex unit cells containing several elementary blocks can be easily implemented in the formalism presented here by simply incorporating the complex EBCs varying along x_1 and spanning over several a_0's in Eqs. (21) and (23). The calculated band structure for this crystal is shown in Fig. 3(c). One expects an additional folding of the frequency bands due to the longer (double) lattice constant, and this is indeed the picture observed. We note in passing that in this hybrid crystal combining grounded and floating-potential EBCs, the A_1-like branch practically coincides with the corresponding branch of the grounded crystal [Fig. 3(b)]. The cutoff frequency of this Lamb-like guided mode originates from the resonance condition of the transverse modes along the plate thickness, $f_{A_1}=\frac{v_{3T}}{2h}=\frac{1}{2h}\sqrt{\frac{c_{44}^E}{\rho}}=0.42$ MHz. Our results shown in Fig. 3 are in excellent agreement with finite element calculations [65] (open symbols); in the most demanding case, $n_{\max}=30$ terms in the Fourier series are needed to obtain convergence better than 10^{-4}.

B. Resonant inductance loading

In all cases examined up to now, the hybridization gaps originate from the avoided crossing between bands of the same symmetry corresponding to the Lamb-like modes of the phononic crystal plate, but no resonance modes are induced by the impedance loads. This can be achieved if, for instance, an inductance load L is introduced on the one-side electrodes (let us assume $Z^{\rm u}=\mathrm{i}L\omega$ and $Z^{\rm d}=0$). Since, naturally, the piezoelectric plate can be effectively described by a planar capacitor C whose surfaces are parallel to x_1x_2 plane, this configuration results in an equivalent—in the simplest case—LC circuit possessing an electric resonance frequency $f_0=\frac{1}{2\pi\sqrt{LC}}$. C is an intrinsic to the piezoelectric plate parameter, which can be determined as described in Ref. [39]. Bringing together the isolated LC circuits to form a crystal, we obtain due to interactions of the resonances of the elementary LC circuits, described equivalently by a transmission line model [39], a dispersive coslike resonant band

$$\sin\frac{k_1a}{2}=\sqrt{\frac{C}{4C'}\left[\left(\frac{\omega_0}{\omega}\right)^2-1\right]}, \tag{28}$$

which extends from $f_0=\frac{\omega_0}{2\pi}$ to $f_\pi=f_0(4\frac{C'}{C}+1)^{-1/2}<f_0$ at the center ($k_1=0$) and at the edge ($k_1=\frac{\pi}{a}$), respectively, of the first BZ. Here, C' corresponds to a planar capacitor whose surfaces are parallel to x_1x_3 plane, accounting for all piezoelectric effects appearing when adjacent electrodes have different electric charge distributions due to nonzero values of the Bloch wave vector k_1.

The calculated band structure for such an infinite phononic crystal ($a=a_0$, with inductance loads on the upper side electrodes) is shown in Fig. 4 for three different values of $L=235$ μH, 470 μH, and, 940 μH. The dispersion relation follows the picture of the corresponding grounded phononic crystal [Fig. 3(b)] on which the dispersive, unhybridized, resonant band Eq. (28), shown by dotted lines in Fig. 4, is superimposed. It crosses, for the cases shown here, the S_0- and A_0-like branches, thus leading to avoided-crossing (hybridization) band gaps, easy to tune electrically through

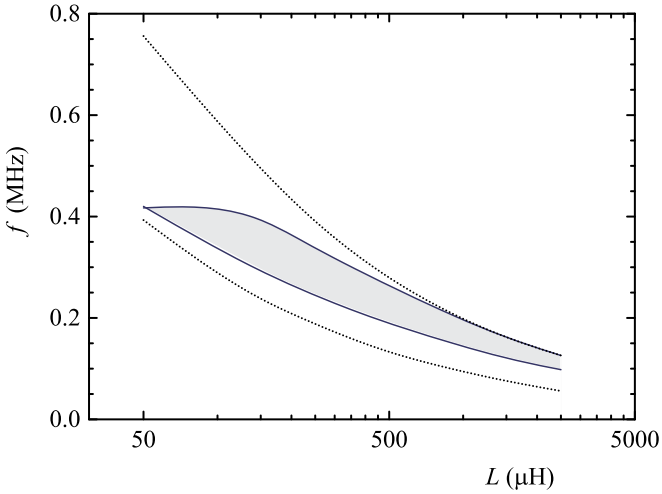

FIG. 5. Variation of the width of the hybridization gap (shaded area), originating from the interaction of the electromagnetic resonant and S_0-like modes, with the inductance load L, for the phononic crystal described in Fig. 4. The dotted lines represent the frequency limits of the resonant band, f_0 and f_π, at the center and at the edge of the first BZ, respectively.

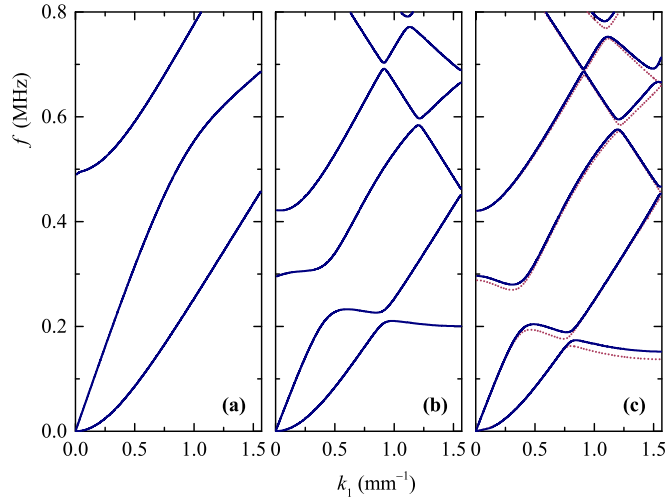

FIG. 6. Calculated frequency band structure of the infinite one-dimensional inductance-loaded phononic crystal plate ($L = 470\ \mu$H), as described in Fig. 4(b), for three different values of the truncation order: (a) $n_{\max} = 0$, (b) $n_{\max} = 1$, and, (c) $n_{\max} = 5$. In (c) the full calculation of Fig. 4(b) ($n_{\max} = 30$) is also reproduced for comparison (red dotted lines).

the value of L. We note in passing that in the case of the inductance-loaded plate, avoided-crossing effects (though weak) are also observed every time two Lamb-like bands cross each other. The most important in width is, however, the band gap originating from the hybridization of the electric resonance mode with the S_0-like branch. Its width increases with decreasing L as depicted in Fig. 5. For low L values, this gap closes down, and another one originating from the interaction of the electric mode with the A_1 branch opens up at frequencies higher than 0.42 MHz.

The case of resonant-inducing dipole loads offers a nice example for the study of the role of the diffracted beams (n-components in the expansion sums of the wave fields) in the formation of the band structure diagram of these crystals. In Fig. 6(a), we present the band-structure calculation for the inductance-loaded crystal ($L = 470\ \mu$H) described in Fig. 4(b), performed by keeping only the central beam ($n_{\max} = 0$) in the corresponding sums of the expressions of the wave fields. The picture obtained coincides with the dispersion plot of the corresponding homogeneous PZT plate (i.e., if all metallic strips and loadings are removed), for which the EBC is $D_3 = D_3^v$ at every point on the surface, instead of Eqs. (11) and (12). The S_0-like band exhibits a linear dispersion at $\omega \to 0$ (long-wavelength limit) with an effective medium slope $c_{\text{eff}} = 4110$ m s^{-1}, and the A_1-like cutoff frequency occurs at 0.49 MHz. As expected, no folding of the frequency bands at the edges of the BZ is observed, because of the absence of the diffracted beams. For the same reason, all the effects originating from the electric resonance are erased. Introducing in the calculation the first "shell" of reciprocal-lattice vectors ($\mathbf{g}_1 = \pm\frac{2\pi}{a}\hat{\mathbf{x}}_1$) that corresponds to the truncation order $n_{\max} = 1$ already provides a picture of the band diagram [see Fig. 6(b)] very close to the final converged calculation, given in Fig. 4(b). The effective-medium slope at $\omega \to 0$ is calculated to be $c_{\text{eff}} = 3710$ m s^{-1} and the A_1-like cutoff frequency occurs at 0.42 MHz. The electric-resonance band extending from $f_0 = 0.296$ MHz ($k_1 = 0$) to $f_\pi = 0.200$ MHz ($k_1 = \frac{\pi}{a}$) is well formed and all expected band-foldings appear in the band diagram. In Fig. 6(c), the corresponding calculation including 11 reciprocal lattice vectors ($n_{\max} = 5$) reveals slight corrections in the general picture, the most important being the dispersion of the electric resonant band that now extends from $f_0 = 0.288$ MHz ($k_1 = 0$) to $f_\pi = 0.152$ MHz ($k_1 = \frac{\pi}{a}$). The edge f_π of this band is strongly affected by the contribution of the reciprocal-lattice vectors $\mathbf{g}_n$ in the wave-field sums, and this image implies, in accordance to the transmission-line simplified model, that intercellular interactions described effectively by the capacitance C' cannot be correctly accounted for if a sufficient number of diffracted beams is not taken into account. The effective medium slope of the S_0-like mode becomes $c_{\text{eff}} = 3670$ m s^{-1} in agreement with the value obtained from the full calculation ($n_{\max} = 30$) of Fig. 4(b), represented here by red dotted lines for comparison.

C. Cell-interconnecting EBCs

We close this discussion with a simple example of interconnected adjacent electrodes through an impedance load, as depicted in Fig. 2(c). Precisely, we add to the case of inductance loaded electrodes, $Z^{\text{u}} = \text{i}L\omega$, discussed previously (Sec. III B), a capacitance $Z^a = 1/\text{i}C_a\omega$. It is worth remembering that, following the transmission line model of Ref. [39], Z^{u} is connected in parallel to the effective piezoelectric capacitor C, while Z^a is connected in parallel to the effective piezoelectric capacitor C'. Then it is straightforward to show that the dispersion relation describing the relatively flat resonant band of Eq. (28) is still valid if C' is replaced by $C' + C_a$. Considering negative values for the capacitance C_a, we can tune the lower frequency of the resonant band, f_π, located at the edge of the BZ, shifting its position at higher frequencies. Obviously, the limit of the resonant band at the center of the

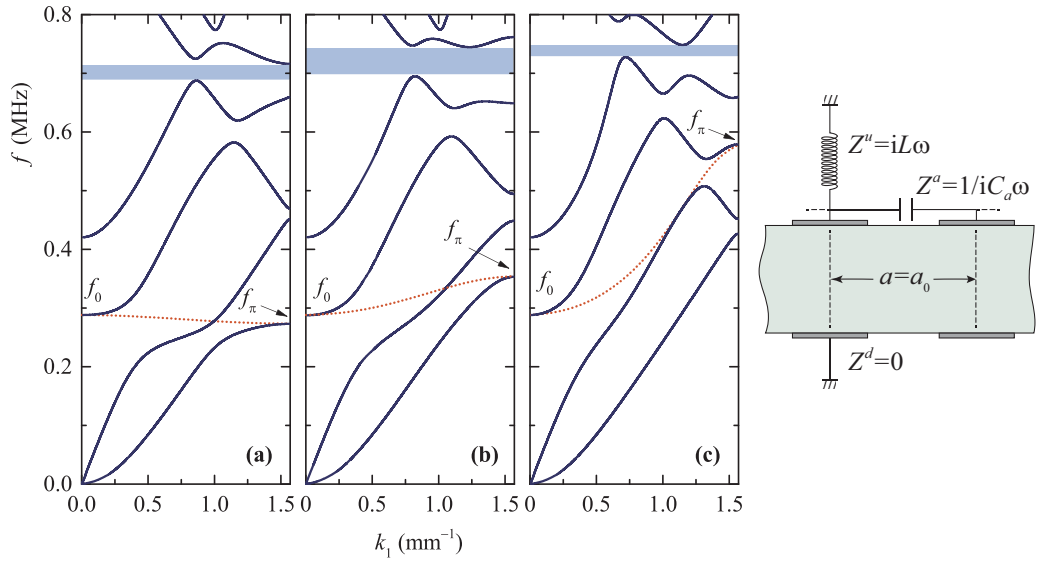

FIG. 7. Calculated frequency band structure of an infinite one-dimensional phononic crystal plate, as described in Fig. 3, but with asymmetric EBCs applied shown in the right margin, consisting of grounded electrodes at the lower plate surface ($Z^{\rm d}=0$) and, at the upper plate surface, inductance loaded electrodes ($Z^{\rm u}=\mathrm{i}L\omega$) interconnected through a capacitance ($Z^a=1/\mathrm{i}C_a\omega$), following the combination of Fig. 2(c). A significant modification of the initial electric-resonance band [in the absence of C_a, Fig. 4(b)] is shown for three different values of negative capacitance: (a) $C_a=-0.55$ nF, (b) $C_a=-0.675$ nF, and (c) $C_a=-0.825$ nF, altering its frequency limit f_π, at the edge of the BZ, while the frequency limit f_0 at the center of the BZ is univocally determined by the inductance $L=470$ μH. The dotted lines represent the electric resonance bands before hybridization (see text) and the shaded areas denote absolute gap regions.

BZ, f_0, is exclusively determined by the choice of the inductance load. Let us consider the case of Fig. 4(b) as a reference system, for which $L=470$ μH with $f_0=0.288$ MHz and $f_\pi=0.137$ MHz as deduced from the full calculation, thus leading to $C=0.649$ nF and $C'=0.551$ nF for the intrinsic piezoelectric capacitances along the directions x_3 and x_1, respectively.

In Fig. 7, we plot the frequency band structure of the phononic crystal plate whose unit cell is shown in Fig. 2(c), for three different negative values of the capacitance C_a, namely -0.55 nF, which is close to the value of $-C'$ of the reference system [see Fig. 7(a)], and, -0.675 nF and -0.825 nF, which are lower than the value of $-C'$ of the reference system [see Fig. 7(b),7(c)]. In the first case, as expected, we observe $f_\pi=0.273$ MHz to be very close to f_0, implying a flat electric resonant band before hybridization [shown by dotted lines in Fig. 7(a)], since $C'+C_a\approx 0$. We note here that C' is in reality slightly changed with respect to the reference value, as we can confirm from $f_\pi=f_0(4\frac{C'+C_a}{C}+1)^{-1/2}$, finding $C'=0.568$ nF. As a result of the interaction of the flat resonant electric band with the S_0-like and A_0-like bands, two oblique avoided-crossing (hybridization) gaps are observed, centered at about 0.28 MHz and 0.27 MHz, respectively.

Decreasing further the interconnecting capacitance C_a, as shown in Figs. 7(b) and 7(c), results in a significant modification of its slope ($f_\pi>f_0$). From the full elastodynamic band-structure calculation, we estimate, after careful analysis of the bands shape as compared to the reference system [Fig. 4(b)], $f_\pi=0.353$ MHz [for $C_a=-0.675$ nF, Fig. 7(b)] and $f_\pi=0.579$ MHz [for $C_a=-0.825$ nF, Fig. 7(c)], and, following the simplified electric-line model, we deduce from $C'=[(\frac{f_0}{f_\pi})^2-1]\frac{C}{4}-C_a$ the intrinsic values to be $C'=0.621$ nF and $C'=0.703$ nF, respectively. We observe that C' varies significantly, as the slope of the unhybridized electric resonant band (dotted lines in Fig. 7), estimated from Eq. (28), increases. This can be explained by a qualitative picture: the more dispersive the resonant band is, the stronger the interactions are between adjacent cells, thus leading to higher C' values, accounting for stronger piezoelectric coupling effects along x_1 direction. Finally, a common feature for all cases examined here, assuming negative values for C_a, in accordance with the previous comment, is the stronger avoided-crossing interaction as compared to the reference system that leads to much wider band gaps in general, and to the appearance of absolute frequency band gaps, highlighted by the shaded regions in Fig. 7.

IV. CONCLUSIONS

In conclusion, we presented a full elastodynamic theoretical model involving piezoelectric effects in piezoceramic plates structured periodically with metallic strip arrays at their surface, coupled with external circuit loads. These systems constitute a powerful, yet unexplored, alternative to their complementary companion: the piezoelectric patch arrays, offering ease of fabrication combined to ease in the electric command to produce tunable elastodynamic response. We have shown that an additional degree of freedom relying on interconnected electrodes can modulate the shape of the resonant band that hybridize with the plate's Lamb eigenmodes, resulting in a dramatically modified picture for the dispersion relation of these systems. A plethora of possible external electric-circuit configurations can be imagined and modeled with the formalism proposed in this paper, thus offering a handy tool to tailor the dispersion properties of this kind of

periodically structured wave guides. In the near future, an extension of our method to include the transmission and reflection properties of elastic waves through such piezoelectric plates should be realized, accompanied to appropriate modifications for transforming the nonlinear system providing the Lamb-like dispersion relation to a typical linear eigenvalue problem. Piezoelectric phononic crystal plates of higher dimensions, i.e., with 2D metallic arrays on their surface, can be easily modeled by a more or less straightforward generalization of our theoretical approach.

ACKNOWLEDGMENT

F.-H.C.-B. was supported by the Normandy Region RIN Program METACAP through a postgraduate fellowship.

APPENDIX A: ELEMENTARY SOLUTIONS OF A BULK PIEZOCERAMIC MATERIAL

We will adapt and apply the basic formalism of piezoelectricity to the case of PZT piezoceramics, whose specific 6*mm* symmetry leads to the following explicit forms for the elastic, piezoelectric, and dielectric tensors:

$$\overleftrightarrow{c}^E = \{c^E_{pq}\} = \begin{bmatrix} c^E_{11} & c^E_{12} & c^E_{13} & 0 & 0 & 0 \\ c^E_{12} & c^E_{11} & c^E_{13} & 0 & 0 & 0 \\ c^E_{13} & c^E_{13} & c^E_{33} & 0 & 0 & 0 \\ 0 & 0 & 0 & c^E_{44} & 0 & 0 \\ 0 & 0 & 0 & 0 & c^E_{44} & 0 \\ 0 & 0 & 0 & 0 & 0 & c^E_{66} \end{bmatrix}, \quad \text{(A1)}$$

$$\overleftrightarrow{e} = \{e_{ip}\} = \begin{bmatrix} 0 & 0 & 0 & 0 & e_{15} & 0 \\ 0 & 0 & 0 & e_{15} & 0 & 0 \\ e_{31} & e_{31} & e_{33} & 0 & 0 & 0 \end{bmatrix}, \quad \text{(A2)}$$

$$\overleftrightarrow{\epsilon}^S = \{\epsilon^S_{ij}\} = \begin{bmatrix} \epsilon^S_{11} & 0 & 0 \\ 0 & \epsilon^S_{11} & 0 \\ 0 & 0 & \epsilon^S_{33} \end{bmatrix}, \quad \text{(A3)}$$

with $c^E_{66} = \frac{c^E_{11}-c^E_{12}}{2}$. We have adopted compact subscript notation, i.e., $p, q = 1, 2, 3, 4, 5, 6$ stand for $ij, kl = 11, 22, 33, 23$ (or 32), 31 (or 13), 12 (or 21), respectively.

Combining the constitutive equations of piezoelectricity Eqs. (1) and (2) to the stress equation of motion (we assume monochromatic waves of angular frequency ω with a $e^{+i\omega t}$ time dependence),

$$T_{ij,i} = \rho\ddot{u}_j = -\rho\omega^2 u_j, \quad \text{(A4)}$$

and the charge equation of electrostatics

$$D_{i,i} = 0, \quad \text{(A5)}$$

we obtain with the help of Eqs. (5), (6), and (A1)–(A3) a set of four equations containing the generalized elastic field components and their second partial derivatives. Assuming plane-wave solutions of the form $u_i = B_i e^{-i\omega(s_1x_1+s_2x_2+s_3x_3)}$, with $i = 1, 2, 3, 4$ (we recall that $u_4 \equiv \varphi$), where s_i, $i = 1, 2, 3$, are the slowness vector components defined by $\mathbf{k} = \omega\mathbf{s}$, $\mathbf{k}$ being the wave vector and B_i appropriate coefficients to be determined. If we restrict the propagation in x_1x_3 plane (i.e., we put $s_2 = 0$), the system of four equations takes the following symmetric and block-diagonal matrix form:

$$\begin{bmatrix} m_{11} & m_{12} & m_{13} & 0 \\ m_{12} & m_{22} & m_{23} & 0 \\ m_{13} & m_{23} & m_{33} & 0 \\ 0 & 0 & 0 & m_0 \end{bmatrix} \begin{bmatrix} B_1 \\ B_3 \\ B_4 \\ B_2 \end{bmatrix} = \begin{bmatrix} 0 \\ 0 \\ 0 \\ 0 \end{bmatrix}, \quad \text{(A6)}$$

where

$$\begin{aligned} m_{11} &= c^E_{11}s_1^2 + c^E_{44}s_3^2 - \rho, \quad m_{12} = \left(c^E_{13} + c^E_{44}\right)s_1s_3, \\ m_{13} &= (e_{31} + e_{15})s_1s_3, \quad m_{22} = c^E_{44}s_1^2 + c^E_{33}s_3^2 - \rho, \\ m_{23} &= e_{15}s_1^2 + e_{33}s_3^2, \quad m_{33} = -\left(\epsilon^S_{11}s_1^2 + \epsilon^S_{33}s_3^2\right), \\ m_0 &= c^E_{66}s_1^2 + c^E_{44}s_3^2 - \rho. \end{aligned} \quad \text{(A7)}$$

The special form of Eq. (A6) implies two independent subspaces corresponding to uncoupled eigenmodes: the out-of-plane (SH) modes with respect to the x_1x_3 plane of propagation vibrating along x_2 axis, described by the scalar equation $m_0B_2 = 0$, and the in-plane vibrations lying on x_1x_3 plane, described by the 3×3 subsystem,

$$\mathbf{M}\left(s_3^{(p)}\right)\mathbf{B}^{(p)} = \mathbf{0}, \quad \text{(A8)}$$

where $\mathbf{M} = \{m_{ij}\}$ is the symmetric matrix with elements given in Eq. (A7) and $\mathbf{B}^{(p)} = [B_1^{(p)}, B_3^{(p)}, B_4^{(p)}]^t$. Only the in-plane vibrations will concern us here. The system Eq. (A8) does not depend on ω and constitutes a nonlinear eigenvalue problem with eigenvalues $s_3^{(p)}$ and corresponding eigenvectors $\mathbf{B}^{(p)}$, the index $p = 1, 2, 3$ denoting the pth eigenvalue. Both $s_3^{(p)}$ and $\mathbf{B}^{(p)}$ can be determined analytically for a given value of s_1. The condition $\det\mathbf{M} = 0$ leads to a third-degree polynomial of variable s_3^2,

$$\alpha s_3^6 + \beta s_3^4 + \gamma s_3^2 + \delta = 0, \quad \text{(A9)}$$

with solutions the following three eigenvalues $s_3^{(p)}$, $p = 1, 2, 3$ (as well as their opposites and/or conjugates):

$$\begin{aligned} s_3^{(1)} &= \sqrt{\left(\Delta - \frac{3\alpha\gamma - \beta^2}{\Delta} - \beta\right)\frac{1}{3\alpha}}, \\ s_3^{(2)} &= \sqrt{\left(-e^{-i\frac{\pi}{3}}\Delta + e^{+i\frac{\pi}{3}}\frac{3\alpha\gamma - \beta^2}{\Delta} - \beta\right)\frac{1}{3\alpha}}, \\ s_3^{(3)} &= \sqrt{\left(-e^{+i\frac{\pi}{3}}\Delta + e^{-i\frac{\pi}{3}}\frac{3\alpha\gamma - \beta^2}{\Delta} - \beta\right)\frac{1}{3\alpha}}, \end{aligned} \quad \text{(A10)}$$

where

$$\begin{aligned} \Delta = \Bigg\{ &\left[\left(-\frac{27}{2}\alpha^2\delta + \frac{9}{2}\alpha\beta\gamma - \beta^3\right)^2 + (3\alpha\gamma - \beta^2)^3\right]^{1/2} \\ &- \frac{27}{2}\alpha^2\delta + \frac{9}{2}\alpha\beta\gamma - \beta^3\Bigg\}^{1/3}. \end{aligned} \quad \text{(A11)}$$

The explicit expressions of the coefficients in Eq. (A9) are given below:

$$\begin{aligned}
\alpha &= \rho^{-2}c_{44}^{E}\left(c_{33}^{E}+\frac{e_{33}^{2}}{\epsilon_{33}^{S}}\right),\\
\beta &= \rho^{-2}\Bigg[-c_{13}^{E}\left(c_{13}^{E}+2c_{44}^{E}+2\frac{e_{33}(e_{31}+e_{15})}{\epsilon_{33}^{S}}\right)+c_{33}^{E}\frac{(e_{31}+e_{15})^{2}}{\epsilon_{33}^{S}}\\
&\quad+c_{44}^{E}\left(\frac{\epsilon_{11}^{S}}{\epsilon_{33}^{S}}c_{33}^{E}-\frac{2e_{31}e_{33}}{\epsilon_{33}^{S}}\right)+c_{11}^{E}\left(c_{33}^{E}+\frac{e_{33}^{2}}{\epsilon_{33}^{S}}\right)\Bigg]s_{1}^{2}-\rho^{-1}\left(c_{44}^{E}+c_{33}^{E}+\frac{e_{33}^{2}}{\epsilon_{33}^{S}}\right),\\
\gamma &= \rho^{-2}\Bigg[c_{11}^{E}\frac{2e_{15}e_{33}}{\epsilon_{33}^{S}}+\frac{\epsilon_{11}^{S}}{\epsilon_{33}^{S}}\left(c_{11}^{E}c_{33}^{E}-{c_{13}^{E}}^{2}-2c_{13}^{E}c_{44}^{E}\right)-c_{13}^{E}\frac{2e_{15}(e_{31}+e_{15})}{\epsilon_{33}^{S}}+c_{44}^{E}\left(c_{11}^{E}+\frac{e_{31}^{2}}{\epsilon_{33}^{S}}\right)\Bigg]s_{1}^{4}\\
&\quad-\rho^{-1}\left[c_{11}^{E}+c_{44}^{E}+\frac{\epsilon_{11}^{S}}{\epsilon_{33}^{S}}\left(c_{33}^{E}+c_{44}^{E}\right)+\frac{2e_{15}e_{33}+(e_{31}+e_{15})^{2}}{\epsilon_{33}^{S}}\right]s_{1}^{2}+1,\\
\delta &= \frac{\epsilon_{11}^{S}}{\epsilon_{33}^{S}}\left[\rho^{-2}c_{11}^{E}\left(c_{44}^{E}+\frac{e_{15}^{2}}{\epsilon_{11}^{S}}\right)s_{1}^{6}-\rho^{-1}\left(c_{11}^{E}+c_{44}^{E}+\frac{e_{15}^{2}}{\epsilon_{11}^{S}}\right)s_{1}^{4}+s_{1}^{2}\right].
\end{aligned}\tag{A12}$$

APPENDIX B: UNIT-CELL INTEGRALS

The coefficients γ_{nm}^{ν} appearing in the EBCs [Eq. (26)] include all external circuit information through the impedances Z^{ν} and result from the integration over the unit-cell region along x_1 through the quantities α_{nm} and β_{nm}. Their explicit expressions are

$$\gamma_{nm}^{\nu}=\frac{1}{\epsilon_0 k_1}\left[\left(1+\frac{1}{\mathrm{i}\omega Z^{\nu}\mathcal{A}\epsilon_0 k_1}\right)^{-1}\alpha_{nm}+\beta_{nm}\right],\tag{B1}$$

where

$$\alpha_{nm}=w\mathcal{P}_n(k_1)\mathcal{P}_m(k_1),\tag{B2}$$

$$\beta_{nm}\equiv\left(\int_{-\frac{a}{2}}^{-\frac{w}{2}}+\int_{\frac{w}{2}}^{\frac{a}{2}}\right)dx_1\mathrm{e}^{-\mathrm{i}\omega(s_{1n}-s_{1m})x_1}=a\delta_{nm}-w\mathcal{P}_{n-m}(k_1=0),\tag{B3}$$

and

$$\mathcal{P}_n(k_1)\equiv\frac{1}{w}\int_{-\frac{w}{2}}^{+\frac{w}{2}}dx_1\mathrm{e}^{-\mathrm{i}\omega s_{1n}x_1}=\frac{\sin\left(\omega s_{1n}\frac{w}{2}\right)}{\omega s_{1n}\frac{w}{2}},\tag{B4}$$

with $\omega s_{1n}=k_1+g_n=k_1+\frac{2\pi}{a}n$.

[1] *Acoustic Metamaterials and Phononic Crystals*, edited by P. A. Deymier, Springer Series in Solid-State Sciences Vol. 173 (Springer, Berlin, 2013).

[2] *Phononic Crystals: Fundamentals and Applications*, edited by A. Khelif and A. Adibi (Springer, New York, 2016).

[3] J. Yu, S. Mitrovic, D. Tham, J. Varghese, and J. Heath, Nat. Nanotechnol. **5**, 718 (2010).

[4] Z. Yang, F. Gao, X. Shi, X. Lin, Z. Gao, Y. Chong, and B. Zhang, Phys. Rev. Lett. **114**, 114301 (2015).

[5] M. Miniaci, R. K. Pal, B. Morvan, and M. Ruzzene, Phys. Rev. X **8**, 031074 (2018).

[6] A. A. Maznev, A. G. Every, and O. B. Wright, Wave Motion **50**, 776 (2013).

[7] G. Trainiti and M. Ruzzene, New J. Phys. **18**, 083047 (2016).

[8] C. Croenne, J. O. Vasseur, O. B. Matar, M. F. Ponge, P. A. Deymier, A. C. Hladky-Hennion, and B. Dubus, Appl. Phys. Lett. **110**, 061901 (2017).

[9] *Metamaterials: Theory, Design, and Applications*, edited by T. J. Cui, D. R. Smith, and R. P. Liu (Springer, New York, 2010).

[10] *Tutorials in Metamaterials*, edited by M. A. Noginov and V. A. Podolskiy (CRC Press, Boca Raton, 2011).

[11] M. Sigalas and E. N. Economou, J. Sound Vib. **158**, 377 (1992).

[12] M. S. Kushwaha, P. Halevi, L. Dobrzynski, and B. Djafari-Rouhani, Phys. Rev. Lett. **71**, 2022 (1993).

[13] Z. Y. Liu, X. X. Zhang, Y. W. Mao, Y. Y. Zhu, Z. Y. Yang, C. T. Chan, and P. Sheng, Science **289**, 1734 (2000).

[14] S. A. Cummer, B. I. Popa, D. Schurig, D. R. Smith, J. Pendry, M. Rahm, and A. Starr, Phys. Rev. Lett. **100**, 024301 (2008).

[15] B. Rostami-Dogolsara, M. K. Moravvej-Farshi, and F. Nazari, Phys. Rev. B **93**, 014304 (2016).

[16] S. Amoudache, R. Moiseyenko, Y. Pennec, B. Djafari-Rouhani, A. Khater, R. Lucklum, and R. Tigrine, J. Appl. Phys. **119**, 114502 (2016).

[17] A. Khelif, B. Djafari-Rouhani, J. O. Vasseur, P. A. Deymier, Ph. Lambin, and L. Dobrzynski, Phys. Rev. B **65**, 174308 (2002).

[18] J. H. Sun and T. T. Wu, Phys. Rev. B **71**, 174303 (2005).

[19] F. L. Hsiao, A. Khelif, H. Moubchir, A. Choujaa, C. C. Chen, and V. Laude, Phys. Rev. E **76**, 056601 (2007).

[20] S. Yang, J. H. Page, Z. Y. Liu, M. L. Cowan, C. T. Chan, and P. Sheng, Phys. Rev. Lett. **93**, 024301 (2004).

[21] M. Ke, Z. Y. Liu, C. Y. Qiu, W. Wang, J. Shi, W. Wen, and P. Sheng, Phys. Rev. B **72**, 064306 (2005).

[22] A. Khelif, P. Deymier, B. Djafari-Rouhani, J. Vasseur, and L. Dobrzynski, J. Appl. Phys. **94**, 1308 (2003).

[23] K. Bertoldi and M. C. Boyce, Phys. Rev. B **77**, 052105 (2008).

[24] J. Y. Yeh, Physica B **400**, 137 (2007).

[25] J. F. Robillard, O. B. Matar, J. Vasseur, P. Deymier, M. Stippinger, A. C. Hladky-Hennion, Y. Pennec, and B. Djafari-Rouhani, Appl. Phys. Lett. **95**, 124104 (2009).

[26] Z. Xu, F. Wu, and Z. Guo, Solid State Commun. **154**, 43 (2013).

[27] A. Sato, Y. Pennec, N. Shingne, T. Thurn-Albrecht, W. Knoll, M. Steinhart, B. Djafari-Rouhani, and G. Fytas, ACS Nano **4**, 3471 (2010).

[28] C. Xu, F. Cai, S. Xie, F. Li, R. Sun, X. Fu, R. Xiong, Y. Zhang, H. Zheng, and J. Li, Phys. Rev. Appl. **4**, 034009 (2015).

[29] O. Thorp, M. Ruzzene, and A. Baz, Smart Mater. Struct. **10**, 979 (2001).

[30] A. Spadoni, M. Ruzzene, and K. Cunefare, J. Intell. Mater. Syst. Struct. **20**, 979 (2009).

[31] F. Casadei, T. Delpero, A. Bergamini, P. Ermanni, and M. Ruzzene, J. Appl. Phys. **112**, 064902 (2012).

[32] Y. Huang, H. M. Wang, and W. Q. Chen, J. Appl. Phys. **115**, 133501 (2014).

[33] Y. Huang, C. L. Zhang, and W. Q. Chen, J. Appl. Mech. **81**, 081005 (2014).

[34] Y. Y. Chen, G. L. Huang, and C. T. Sun, J. Vib. Acoust. **136**, 061008 (2014).

[35] S. Degraeve, C. Granger, B. Dubus, J. O. Vasseur, M. Pham Thi, and A.-C. Hladky-Hennion, J. Appl. Phys. **115**, 194508 (2014).

[36] S. Degraeve, C. Granger, B. Dubus, J. O. Vasseur, M. Pham Thi, and A.-C. Hladky-Hennion, Smart Mater. Struct. **24**, 085013 (2015).

[37] S.-A. Mansoura, P. Benard, B. Morvan, P. Marechal, A.-C. Hladky-Hennion, and B. Dubus, Smart Mater. Struct. **24**, 115032 (2015).

[38] N. Kherraz, L. Haumesser, F. Levassort, P. Benard, and B. Morvan, Appl. Phys. Lett. **108**, 093503 (2016).

[39] N. Kherraz, L. Haumesser, F. Levassort, P. Benard, and B. Morvan, J. Appl. Phys. **123**, 094901 (2018).

[40] C. Vasseur, C. Croenne, J. O. Vasseur, B. Dubus, M. P. Thi, C. Prevot, and A. C. Hladky-Hennion, IEEE Trans. Ultrason., Ferroelectr., Freq. Control **65**, 1552 (2018).

[41] M. Alami, E. H. El Boudouti, B. Djafari-Rouhani, Y. El Hassouani, and A. Talbi, Ultrasonics **90**, 80 (2018).

[42] C. Sugino, M. Ruzzene, and A. Erturk, IEEE/ASME Trans. Mechatronics **23**, 2144 (2018).

[43] I. A. Viktorov, Sov.-Phys. Acoust. **7**, 236 (1962).

[44] R. M. White and F. W. Voltmer, Appl. Phys. Lett. **7**, 314 (1965).

[45] S. V. Biryukov, Y. V. Gulyaev, V. V. Krylov, and V. P. Plessky, *Surface Acoustic Waves in Inhomogeneous Media*, Springer Series on Wave Phenomena Vol. 20 (Springer, Berlin, 1995).

[46] S. Benchabane, A. Khelif, J.-Y. Rauch, L. Robert, and V. Laude, Phys. Rev. E **73**, 065601(R) (2006).

[47] A.-C. Hladky-Hennion, J. Vasseur, B. Dubus, B. Morvan, N. Wilkie-Chancellier, and L. Martinez, IEEE Trans. Ultrason. Ferroelectr. Freq. Control **60**, 2607 (2013).

[48] D. G. Piliposyan, K. B. Ghazaryan, and G. T. Piliposian, Ultrasonics **54**, 644 (2014).

[49] Q. Xue and Y. Shui, IEEE Trans. Ultrason. Ferroelectr. Freq. Control **37**, 13 (1990).

[50] H. F. Tiersten, J. Acoust. Soc. Am. **35**, 234 (1963).

[51] S. G. Joshi and Y. Jin, J. Appl. Phys. **70**, 4113 (1991).

[52] Y. Jin and S. G. Joshi, J. Acoust. Soc. Am. **92**, 914 (1992).

[53] J. L. Bleustein, J. Acoust. Soc. Am. **45**, 614 (1969).

[54] H. F. Tiersten, J. Acoust. Soc. Am. **35**, 53 (1963).

[55] J. Peng, H. Luo, T. He, H. Xu, and D. Lin, Mater. Lett. **59**, 640 (2005).

[56] I. Ben Salah and M. H. Ben Ghozlen, Physics Procedia **2**, 1377 (2009).

[57] J. J. Campbell and W. R. Jones, IEEE Trans. Sonics Ultrason. **15**, 209 (1968).

[58] A. A. Mezheritsky and A. V. Mezheritsky, IEEE Trans. Ultrason. Ferroelectr. Freq. Control **54**, 2662 (2007).

[59] G. Feuillard, M. Lethiecq, Y. Janin, L. Tessier, and L. Pourcelot, IEEE Trans. Ultrason. Ferroelectr. Freq. Control **44**, 194 (1997).

[60] W. P. Mason, *Physical Acoustics and the Properties of Solids* (D. Van Nostrand Co., Princeton, 1958).

[61] D. A. Berlincourt, D. R. Curran, and H. Jaffe, in *Physical Acoustics-Principles and Methods*, Vol. 1, Part A, edited by W. P. Mason (Academic, New York, 1964).

[62] A. H. Nayfeh and H.-T. Chien, J. Acoust. Soc. Am. **91**, 1250 (1992).

[63] C.-H. Yang and D. E. Chimenti, Appl. Phys. Lett. **63**, 1328 (1993).

[64] https://www.meggittferroperm.com/materials/

[65] We used the COMSOL Multiphysics v. 4.4 software to perform the calculations (www.comsol.com. COMSOL AB, Stockholm, Sweden).